



Multi-parameter and multi-objective optimization of stratified OLEDs over wide field-of-view considering thickness tolerance

LINYA CHEN,^{1,2} HONGGANG GU,^{3,4,7}  XIANHUA KE,³ XUENAN ZHAO,³ KE DING,⁵ SHIBO JIAO,⁶ YU GU,⁵ AND SHIYUAN LIU^{1,3,4,8} 

¹School of Optical and Electronic Information, Huazhong University of Science and Technology, Wuhan, Hubei 430074, China

²Innovation Institute, Huazhong University of Science and Technology, Wuhan, Hubei 430074, China

³State Key Laboratory of Digital Manufacturing Equipment and Technology, Huazhong University of Science and Technology, Wuhan, Hubei 430074, China

⁴Optics Valley Laboratory, Hubei 430074, China

⁵Wuhan China Star Optoelectronics Semiconductor Display Technology Co., Ltd., Wuhan, Hubei 430078, China

⁶Shenzhen China Star Optoelectronics Semiconductor Display Technology Co., Ltd., Shenzhen, Guangdong 518132, China

⁷hongganggu@hust.edu.cn

⁸shyliu@hust.edu.cn

Abstract: Poor wide field-of-view (FOV) performances and low production yields are major factors that restrict the application of organic light-emitting diodes (OLEDs) in large-size panels. In this paper, we propose an optimization and analysis method to improve optical performances of stratified OLEDs over wide FOV with consideration of the thickness tolerance in the practical production process. With key optical performance parameters defined using the angle-dependent luminescence spectra, including the external quantum efficiency (*EQE*), current efficiency (*CE*), just noticeable color difference (*JNCD*), and the color coordinates, the optimization of OLEDs over wide FOV is described as a multi-parameter and multi-objective optimization problem which is accomplished by the genetic algorithms (GAs). Further, the thickness tolerance is introduced to improve the structure stability considering thickness fluctuations in the practical production process. Appropriate thickness tolerances can be determined to achieve stable structures for the OLED device by defining and analyzing the distributions of preference regions of the GA output noninferior solutions and the correlation coefficients between the layer thicknesses. Based on the proposed methods, high-throughput simulations are carried out on a typical Green Bottom-emitting OLED (G-BOLED) to design a stable device structure with high-performances. Experimental results demonstrate that compared with the initial device, the performances of the optimized device have been significantly improved, with the *CE* improved by over 30% in the normal direction, the *EQE* improved by over 20%, and the *JNCD* reduced from 4.45 to 1.36 over the whole FOV of 0-60°. In addition, within the thickness fluctuation in the practical process, optimized devices can strictly satisfy the “Best” preferred region, indicating that the structure is more stable against thickness fluctuations in the practical production process. The proposed optimization method can simultaneously improve optical performances over wide FOV and provide a stable structure for stratified OLEDs, and it therefore can be expected to improve the production yields and promote the OLEDs applied to large-size panels.

© 2022 Optica Publishing Group under the terms of the [Optica Open Access Publishing Agreement](#)

1. Introduction

Organic light-emitting diodes (OLEDs) demonstrate “future technology” features, such as thin, fast response, flexible and foldable. It is gradually replacing the last two generations of display

technologies (i.e., Cathode Ray Tube and Liquid Crystal Display) and has become the mainstream for small and medium-size panels [1–4]. However, as the OLED panel size gets larger and larger, the production yield becomes more and more difficult to control, and key performances of OLED devices, such as the angular color shift and efficiency fading, are still poor when exposed to wide field-of-view (FOV) usage scenarios, as shown in Fig. 1. Therefore, it is necessary to optimize the structure of OLEDs to improve the wide FOV optical performances and production yield.

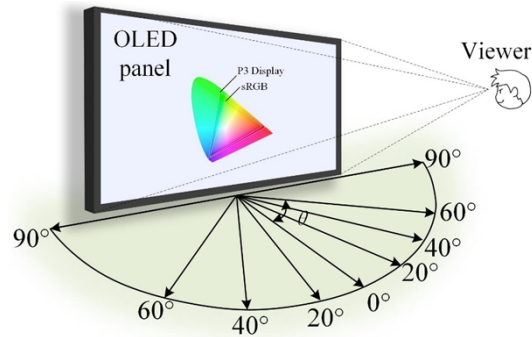


Fig. 1. Schematic diagram of the OLED panel under wide FOV usage scenarios.

Improving the wide FOV optical performances of OLEDs typically comes in three routes: (I) Using high-performance materials, designing different molecular structures and doping. Since the pure organic thermally activated delayed fluorescent (TADF) materials were utilized in OLEDs, the quantum efficiency of the devices has been significantly improved, facilitating the commercialization of OLEDs [5–10]. In addition, designing different molecular structures [11–13] and doping [14] is a very flexible method to enable structure diversity while improving performance. (II) Introducing specific micro-nano structures. Some of them are based on light scattering to improve the wide FOV performances, such as nanohole arrays [15], nanoparticle scattering layers [16] and other quasi-periodic or random structures [17]. Others improve device performance by extracting the energy of coupled waveguide and plasmonic modes in the device through periodic structures, e.g., periodic gratings [18,19], micro lens arrays [20–22]. (III) Designing a reasonable micro-cavity structure via optical optimization. By adding a capping layer on the thin metal cathode [23,24], using transparent conductive oxides [25], and reducing the thickness of the top electrode to increase the transmittance of the top cathode [26–28], the microcavity effect of the OLED device can be changed and the angular color shift can be mitigated. However, new materials are usually developed with long cycles and high costs, and micro-nano structures may bring severe ambiguity effects. Therefore, designing a reasonable micro-cavity structure becomes an essential way. At present, the production yield of mainstream OLED panel manufacturers has reached 60% to achieve break-even [29]. However, it does not guarantee the further improvement of enterprise capacity utilization, which affects the production cost, and then leads to the decline of market share. To the best of our knowledge, there is no effective method yet that can guide the actual production from theory to improve the production yield.

Some interesting works have paid attentions to improving the performances of OLEDs by designing a reasonable micro-cavity structure. For example, C. Lin *et al.* and S. Yoo *et al.* used a blue-detuned micro-cavity structure to obtain low angular dependence but at the expense of efficiency [30,31]. G. Tan *et al.* systematically analyzed the angular color shift of RGB OLED displays and optimized the structure to reduce the color shift by using advanced optimization algorithms [32]. Nevertheless, they did not consider the actual color coordinate, resulting in significant deviations between the chromaticity of the optimized device and the initial device. F.

So *et al.* proposed a multi-mode structure to suppress the color shift effects, and a nearly 10 μm thick epoxy spacer was introduced at the anode and cathode [28,33]. However, the multi-mode structures increase the size of the OLED. In our previous work, we proposed a collaborative optimization strategy to simultaneously improve the current efficiency and the chromaticity quality in the normal direction but without considering the performance degradation of OLEDs over wide FOV [34]. However, few of these works consider the structure stability in the device design, which has significantly influences on the production yields.

In this work, a multi-parameter and multi-objective optimization and analysis method is proposed to simultaneously improve the key performances of stratified OLEDs over wide FOV, including the external quantum efficiency (*EQE*), current efficiency (*CE*), just noticeable color difference (*JNCD*), and the color coordinates (*CIE_x*, *CIE_y*). Firstly, key parameters of OLEDs over wide FOV are defined with mathematical calculation criteria based on the angle-dependent luminescence spectrum. Then, the optimization process for the OLED device over wide FOV is simplified as an inverse problem with multiple output objectives involving multiple variable parameters, and the genetic algorithm (GA) is employed to finalize the multi-parameter and multi-objective optimization process. In addition, the thickness tolerances are also analyzed from the noninferior solutions obtained by the GA optimization, to ensure the stability of OLED structures over the wide FOV. Finally, high-throughput simulations and experiments are conducted to verify the reliability and effectiveness of the proposed methods.

2. Theory and methods

2.1. Definition of key parameters of stratified OLEDs over wide FOV

In our previous study, we have established a comprehensive optical simulation model for stratified OLEDs by using the electric dipole radiation model, microcavity coherence theory, and transfer matrix method [35]. Based on this model, the angle-dependent luminescence spectrum can be described as

$$I(\theta_{\text{air}}, \lambda) = \Theta \frac{S_z^{\text{TM}}(u, \lambda)}{2\pi n_s \tan(\theta_{\text{air}})} + (1 - \Theta) \frac{S_x^{\text{TE}}(u, \lambda) + S_x^{\text{TM}}(u, \lambda)}{2\pi n_s \tan(\theta_{\text{air}})}, \quad (1)$$

where, Θ stands for the dipole orientation, $S(u, \lambda)$ denotes the emitted power of OLEDs in the air, which is a function of the horizontal wave vector u and wavelength λ , the subscripts x and z respectively indicate the horizontally and vertically oriented dipoles, the superscripts “TM” and “TE” respectively stand for the TM-polarization and the TE-polarization, θ_{air} is the emitting angle in the air, and n_s is the refractive index of the emissive layer. The angle-dependent luminescence spectrum given in the above expression is the basis for defining the following key parameters of stratified OLEDs over wide FOV.

- (I) **External quantum efficiency (*EQE*)**, indicating the ratio of the photons emitted from the device to the electrons injected into the device, is a critical parameter to evaluate the luminous performance of the OLED [36], the calculation formulation can also be got from this citation.
- (II) **Current efficiency (*CE*)** is the ratio of the brightness to the current of the OLED, which is the luminous efficiency, considering the sensitivity of human eyes to different wavelengths of light in the visible range, which can be got from Ref. [34].
- (III) **Chromaticity coordinate** provides an objective description of the luminescent color, and all colors can be described in the CIE 1931 color space (*CIE_x*, *CIE_y*, *Y*) or the CIE 1976 color space (u, v, L). It can be easily calculated by the angle-dependent luminescence spectrum, the calculation formulation can be got from Ref. [34]. It should be noted that the CIE 1931 color space does not give a direct way to estimate the color differences, and

the distance in the chromaticity diagram does not correspond to the degree of difference between the two colors. The variation in chromaticity can be described in the CIE 1976 color space, which can be converted from the CIE 1931 color space according to the following relations

$$u(\theta_{\text{air}}) = \frac{4\text{CIE}x(\theta_{\text{air}})}{-2\text{CIE}x(\theta_{\text{air}}) + 12\text{CIE}y(\theta_{\text{air}}) + 3}, \quad (2)$$

$$v(\theta_{\text{air}}) = \frac{9\text{CIE}x(\theta_{\text{air}})}{-2\text{CIE}x(\theta_{\text{air}}) + 12\text{CIE}y(\theta_{\text{air}}) + 3}, \quad (3)$$

where, u and v represent the color coordinate values in the CIE 1976 color space.

(IV) Just noticeable color difference (JNCD) is a parameter to evaluate the screen's color accuracy, and the smaller *JNCD* value means the more accurate color display [31]. The *JNCD* represents the ratio of the distance between different chromaticity coordinates to the constant 0.004, which can be defined in the CIE 1976 color space as given by

$$JNCD = \frac{\sqrt{(u(\theta_{\text{air}}) - u_0)^2 + (v(\theta_{\text{air}}) - v_0)^2}}{0.004}, \quad (4)$$

where, u_0' and v_0' represent the color coordinate values in the normal direction ($\theta_{\text{air}} = 0$). In general, human eyes are not sensitive to chromaticity changes within the range of *JNCD* less than 4, and the color can be approximated as consistent.

2.2. Multi-objective optimization criterion based on the GA

Usually, the noninferior solutions are widely used in the multi-objective optimization problem, which can be obtained through optimization algorithms. The GA simulates the evolutionary laws of organisms in nature and is more suitable and flexible for complex system optimization than other algorithms, such as the gradient method. Gradient method needs to convert multi-objective optimization problems into single-objective optimization problems by assigning a weight to each sub-objective, which is often difficult to choose. But the GA directly uses the multiple objective function values as the search information avoiding the selection of weights. Since the optimization of OLEDs over wide FOV involves multiple objectives and multiple variables, and it is difficult to be converted into a single-objective optimization. Therefore, it is more appropriate to utilize GA to deal with the multi-parameter and multi-objective optimization problem for OLEDs over wide FOV [37,38].

The multi-objective optimization of OLEDs over wide FOV can be simplified to a multi-objective (including the *EQE*, *CE*, *CIE*, *JNCD*, etc.) and multi-parameter (i.e., thickness of each layer) optimization problem. In this paper, the multi-objective optimization based on the GA is described as follows

$$\text{MOGA} = [F, \mathbf{d}, P_0, M, \varphi]. \quad (5)$$

Herein, P_0 is the size of the initial population. A larger P_0 will improve the ability of the global search and the possibility of converging during the optimization. However, with the increase of P_0 , the calculation time of the algorithm will also increase accordingly. M represents the maximum number of iterations. Smaller M will result in non-convergence of optimization results, while larger M will increase simulation time. φ is the proportion of optimal individuals based on noninferior solutions in multi-objective GA optimization, which also determines the size of the output sample after optimization. These three parameters (P_0 , M , φ) have significant impacts on the optimization results, and their values are various for different optimization cases. Therefore, the determination of these parameters needs to consider the characteristics of the optimization problem. The remaining two parameters are descriptions of the optimization problem, with F

representing the optimization objective, and \mathbf{d} indicating the optimization parameters (i.e., the thickness setting of the OLED stack), which can be described as follows

$$\begin{aligned} \mathbf{V} - \min \quad F(\mathbf{d}) &= [EQE(\mathbf{d}), CE(\mathbf{d}), CIE_x(\mathbf{d}), CIE_y(\mathbf{d}), JNCD(\mathbf{d}), \dots]^T, \\ \mathbf{d} &= [d_1, d_2, \dots, d_M] \\ \text{s.t.} \quad d_m &\in X_m, m = 1, 2, \dots, M \end{aligned} \quad (6)$$

where, V-min represents vector minimization, which means each sub-objective in the optimization objective $F(\mathbf{d}) = [EQE(\mathbf{d}), CE(\mathbf{d}), CIE_x(\mathbf{d}), CIE_y(\mathbf{d}), JNCD(\mathbf{d}), \dots]^T$ is as small as possible. d_m is the optimized parameter describing the thickness of the m -th layer in the OLED device, X_m is the constraint of the multi-objective optimization problem, and M is the total number of layers in the OLED device. Since this paper focuses on applying the GA to deal with the OLED optimization over wide FOV, rather than the GA itself, other parameters involved in the GA, such as fitness function, selection operator, crossover operator, will not be elaborated here.

2.3. Analysis of the film thickness tolerance

In the above described optimization problem of OLEDs over wide FOV, it is challenging to select a solution to guide the practical industrial production directly, mainly for two reasons. The first one is that the output noninferior solutions cannot ensure multiple objectives optimal simultaneously, so it is difficult to make the so-called best choice. The second one is that there will inevitably be thickness fluctuations in the practical production process, and actual structure parameters cannot be ideally matched with the pre-designed values, resulting in a deviation between the actual performance and the simulation predicted performance. That is to say, the structure is not stable enough.

To improve the stability of the structure and reduce the influences of thickness fluctuations in practical production on the performance, the thickness tolerance is introduced to evaluate the robustness of the optimization. In mechanical manufacturing, the tolerance represents the allowable variation of the actual parameter. When the parameter changes within the tolerance, it can meet the requirements of interchange or coordination. Similarly, the thickness tolerance here means a specific range of thickness, within which the performances of the OLED are relatively stable and meet the optimization requirements. The thickness tolerance can be obtained by systematically analyzing the noninferior solutions based on the degree of preference for the optimization objectives. We can define upper and lower thresholds for each optimization objective separately, and divide the corresponding optimization parameters into five preference regions $\Omega_1 \sim \Omega_5$, namely best, better, average, poor, and bad respectively. Depending on the importance of the objective, the preference regions can be described as

$$\Omega_j = \{F_1 | a_1 < F_1 < b_1\} \cap \{F_2 | a_2 < F_2 < b_2\} \dots \cap \{F_i | a_i < F_i < b_i\}. \quad (7)$$

Herein, F_i is the i -th optimization objective and a_i and b_i are respectively the upper and the lower thresholds for the i -th optimization objective. In this work, F_1, F_2, F_3, F_4 , and F_5 represent $CE, JNCD, EQE, CIE_x$, and CIE_y , respectively.

The thickness distributions in different preference regions can be described by normal distribution functions. For a normal distribution, about 99.73% values are in confidence interval $(\mu - 3\sigma, \mu + 3\sigma)$ called the 3σ principle, which is widely used in industrial production. Here, μ is the mathematical expectation, and σ is the standard deviation. To ensure that the thicknesses of layers fall in the interval of the “best range” during practical production, referencing the 3σ

principle, the film thickness tolerance(T) is defined in the following form

$$T_i = [\mu_i - 3\sigma_i, \mu_i + 3\sigma_i]. \tag{8}$$

Herein, i represents the layer index of the film in the OLED structure. However, whether in the laboratory or commercial production process, the actual film thicknesses and the pre-designed values usually cannot perfectly match, and there will be a specific range of fluctuation. Smaller thickness fluctuations can reduce the performance loss, but have higher requirements for the equipment and operation, resulting in higher costs. Considering thickness fluctuations brought by the process, the target value of thickness in the preparation can be defined as

$$d_i^{\text{set}} = \left[\frac{\mu_i - 3\sigma_i}{1 - k}, \frac{\mu_i + 3\sigma_i}{1 + k} \right]. \tag{9}$$

Herein, k is the range of thickness fluctuations in the process.

Further, considering that the film thicknesses in the OLED structure are often related to each other in the optical optimization, the correlation coefficient is introduced to judge the correlation between the film thicknesses of two layers, which can be defined as

$$\text{Corr}(d_i, d_j) = \frac{E[(d_i - E(d_i))(d_j - E(d_j))]}{\sigma_{d_i}\sigma_{d_j}}. \tag{10}$$

Herein, $E(\bullet)$ represents the mathematical expectation. Generally, the correlation coefficients are between -1 and 1 . When $\text{Corr}(d_i, d_j)$ equals 1 (or -1), it means that d_i and d_j are completely positively (or negatively) correlated. $\text{Corr}(d_i, d_j) = 0$ means that there is no linear relationship between d_i and d_j . In addition, the absolute value of the correlation coefficient $|\text{Corr}(d_i, d_j)|$ represents the strength of linear correlation between d_i and d_j . When the thickness of a layer deviates from the central value μ_i of the thickness tolerance, the thickness of other layers needs to be adjusted according to the direction of deviation and the correlation coefficient to ensure the stability of the structure. The flowchart of the proposed multi-objective optimization and analysis strategy for OLEDs is shown in Fig. 2.

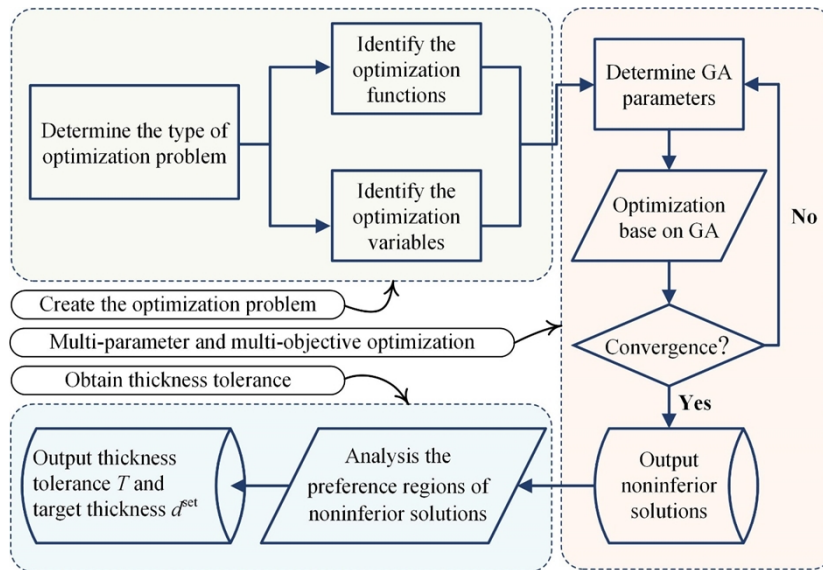


Fig. 2. Flowchart of the proposed multi-objective optimization and analysis strategy for OLED.

3. Experiments

To verify the reliability of the proposed optimization method, experiments are performed on a typical Green Bottom-emitting organic light-emitting diode (G-BOLED), whose structure can be described as air/ Glass/ ITO/ HIL/ HTL/ EBL/ EML/ ETL/EIL/Cathode, as shown in Fig. 3. All the materials involved in the device were provided by Nanjing OLight Optoelectronics Technology Co., Ltd. The optical characteristics, including the optical constants (i.e., the refractive index n and extinction coefficient k) of the materials involved in the device and the inherent luminescence spectrum of the EML are given in Fig. 4. The optical constants and thicknesses are measured by a spectroscopic ellipsometer [39,40](ME-L, Wuhan E-optics Technology Co.).

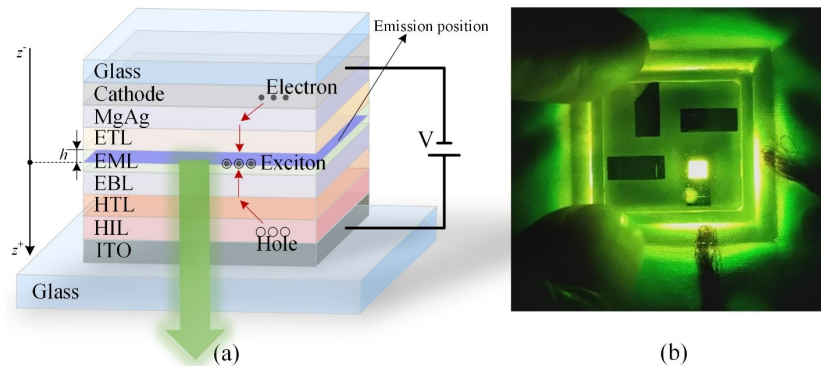


Fig. 3. (a) Schematic diagram of the G-BOLED structure; (b) light-emitting pictures of the G-BOLED under 3 V bias voltage

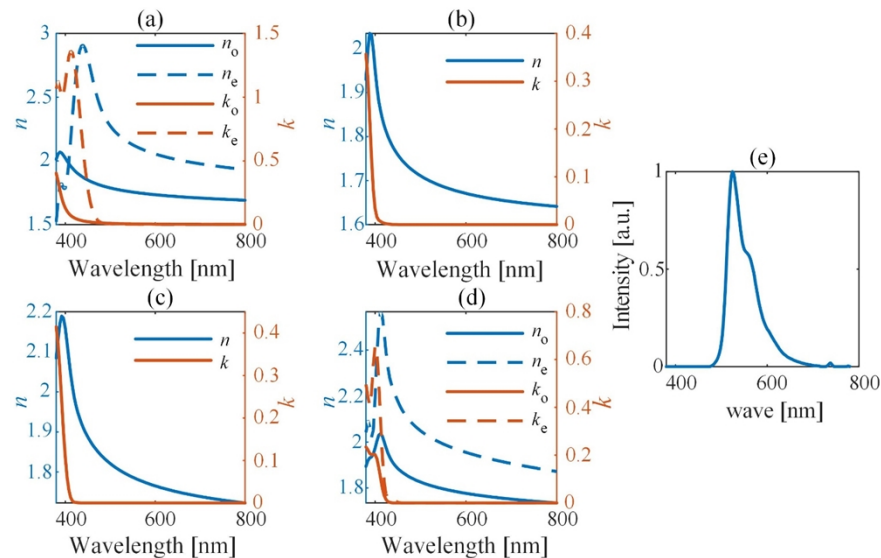


Fig. 4. Intrinsic optical characteristics of the materials involved in the tested G-BOLED. (a)-(d) Optical constants (refractive index n and extinction coefficient k) of layers to be optimized, including the (a) HIL, (b) HTL, (c) EBL, and (d) ETL; (e) inherent spectrum of the EML.

The primary fabrication process for the G-BOLED can be divided into four steps, cleaning the glass substrate with ITO, preparing the evaporation chamber, coating, and packing. The glass

substrate with ITO firstly needs to be ultrasonically cleaned with acetone, ethanol, isopropanol, ultra-pure water for 10 minutes, respectively. Then, it is baked in the oven at 120 °C for 20 minutes. It is important to note that the substrate needs to be purged with nitrogen before being put into and taken out of the oven. Preparation of the evaporation chamber includes setting the vacuum degree of the chamber ($\geq 6.5 \times 10^{-7}$ Torr) and preheating the materials. The deposition order and quality determine the structure and the device performances, respectively. The sequence, temperature, deposition rate, and time must be carefully designed before the deposition. The device packaging is completed in a glove box, where the water and oxygen content must be less than 1 ppm. The air bubbles in the cover plate are squeezed out and then samples are placed in the UV irradiation chamber for 5 minutes.

The wide FOV optical characteristics of the G-BOLED (i.e. angle-dependent luminescence spectrum, *EQE*, *CE*, and *CIE*) are measured by a spectroradiometer (PR-655 Spectra Scan) mounted on an automatic rotation system, when the current density of the device is 10 mA/cm². The *JNCD* is calculated by the *CIE* according to the calculation criterion in Eq. (8). Optical simulations and optimization are performed by the commercial software OFSS 1.0 (Wuhan Yuwei Optical Software Co., Ltd.) and custom-made MATLAB codes based on the proposed method and algorithm. In simulations, the optical characteristics of the OLED are considered, and parameters related to the electrical characteristics, such as the carrier balance rate γ and the probability of exciton recombination χ , are set to be equal to 1. Other parameters required in the simulations, such as the intrinsic quantum efficiency q , dipole distribution function $g(z)$, and dipole orientation parameter θ , are inversely extracted from the angle-dependent luminescence spectra measured by spectroradiometer [41,42].

4. Results and discussion

4.1. Optimization of OLEDs for high optical performances

The thicknesses of the initial device are $\mathbf{d}_{\text{initial}} = [\text{incoherent}, 152, 11.5, 135, 12.7, 37.5, 35.5, 45, 108]$ nm, which are obtained by the spectroscopic ellipsometer. When the current density is 10 mA/cm², the intrinsic radiative quantum efficiency is $q = 0.92$, the dipole distribution function is $g(z) = \delta(0.24)$, the dipole orientation parameter is $\theta = 0.33$, and they are inversely extracted from the measured angle-dependent luminescence spectra. Measured and simulated luminescence spectra in the normal direction and the *CIE* from 0° to 60° are shown in Figs. 5(a) and 5(b). It can be seen that the simulated and experimental results are highly overlapping verifying the accuracy of the proposed method and algorithm. In addition, simulation results for other parameters are, $CE(0^\circ) = 70.66$ cd/A, $EQE = 22.8\%$, $JNCD_{\text{max}} = 7.5$. Obviously, the initial OLED structure has poor performances over wide FOV since $JNCD_{\text{max}} > 4$. This initial OLED is taken as a reference for the following optimization results.

As mentioned above, in the optimization, five objectives, namely the *EQE*, *CE*, *CIE_x*, *CIE_y*, and *JNCD*, should be simultaneously considered to improve OLED performances over wide FOV. The *EQE* and *CE* describe the OLED efficiency from different aspects, to ensure that more photons can be emitted into the air, both *EQE* and *CE* of the optimized device should be higher than those of the initial device. Comparing the OLED efficiency should be performed under the same *CIE*, and an acceptable deviation in color coordinates from the designed values in the normal direction is the basic requirement for the optimization. Here, we defined the constraint condition of the color coordinate in the normal direction as $\Delta CIE_i = |CIE_i^{\text{opt}} - CIE_i^{\text{ini}}| < 0.05$, where superscripts 'opt' and 'ini' represent the optimized and the initial OLEDs respectively, and the subscript i represents x and y . The *JNCD* is an angle-dependent function that can be evaluated by the maximum values within a certain range. This work adopts $JNCD_{\text{max}} < 4$ when the angle changes from 0° to 60° as the acceptable tolerance for the color shift.

The optimization parameters, namely the layer thicknesses, have a huge impact on the key performances of the OLED device, and analyzing the energy distributions with different modes

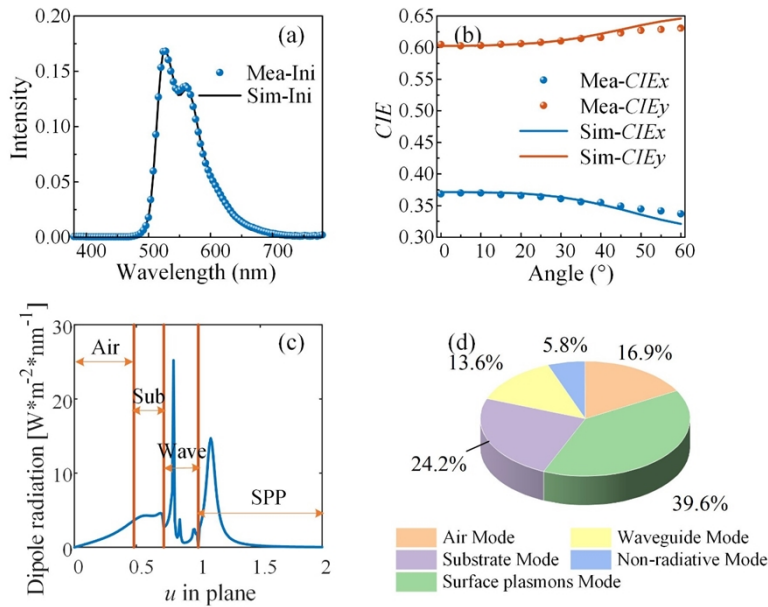


Fig. 5. Key performance parameters of the initial G-BOLED. (a) The outcoupling spectra radiated in the normal direction; (b) color coordinates from 0° to 60° ; (c) energy dissipations at the peak wavelengths; (d) energy percentage of different modes at the peak wavelengths.

in the OLED structure can help us to determine the most sensitive parameters to be optimized. The decay of excitons can be generally divided into non-radiative decay and radiative decay. The former dissipates energy in the form of heat through internal conversion, without producing photons, corresponding to the non-radiative mode. While the radiative decay converts energy into photons, which can be further divided into four modes according to the range of the normalized in-plane wave vector u : (i) $0 < u < 1/n_s$ corresponds to the energy radiated into the air (Air Mode); (ii) $1/n_s < u < n_{\text{glass}}/n_s$ corresponds to the waveguide mode radiated into the substrate (Substrate Mode); (iii) $n_{\text{glass}}/n_s < u < 1$ corresponds to the waveguide mode coupled inside the device (Waveguide Mode), where n_{or} is the refractive index of the transparent layers, including organic layers and ITO electrode; (iv) $u > 1$ corresponds to the surface plasmon mode (Surface Plasmons Mode). The energy distribution of the initial OLED is shown in Figs. 5(c) and 5(d). It can be observed that only 16.9% of the energy can finally radiate into the air, 13.6% of the energy is coupled in the organic layer and 14.2% of the energy is coupled in the substrate. Generally, the Substrate Mode and Surface Plasmons Mode can be extracted by microlens arrays and gratings, respectively [18,19,21]. The Non-radiative Mode is generated by the interaction between electrons, holes, and excitons in the OLED, which is related to the material and electrical properties of the device, and it is difficult to alleviate by optical methods. The Waveguide Mode is related to the thicknesses and optical constants of transparent layers. Since changing the EML thickness will have non-negligible influences on the dipole distribution of the device, and the ITO thickness is hard to change during the experiment for the purchased glass substrate already contains an ITO layer, in this work, the thicknesses of the ETL, EBL, HTL, and HIL are taken as the optimization parameters. The optimization interval is [5, 200] nm, which includes the first and the second microcavity for the device. In the following content, the optimization parameters are represented by $\mathbf{d} = [d_{\text{ETL}}, d_{\text{EBL}}, d_{\text{HTL}}, d_{\text{HIL}}]$. It should be noted that the changes in the thicknesses of the ETL, EBL, HTL, and HIL will also affect the balance of the injection of holes and electrons, and it will affect the optical performance of the device.

The GA is used to deal with the above multi-objective optimization problem involving multiple parameters. The main parameters in GA are defined as $P_0 = 1500$, $M = 300$, $\varphi = 0.5$. The determination of these parameters has considered convergence and efficiency to avoid premature convergence and local optimality problems. Optimized results of the G-BOLED are shown in Fig. 6. Figure 6(a) shows the distribution of noninferior solutions in $[CE, JNCD, EQE]$ space, in which each colored point refers to a noninferior solution. Black dots represent projections of noninferiority in the coordinate planes. It can be seen that the EQE and CE are positively correlated, and the larger the EQE the larger the CE . Besides, some noninferior solutions can provide high EQE and CE , while the $JNCD$ is larger than 4, which is not ideal. Figure 6(b) shows the distribution of noninferior solutions in $[\Delta CIE_x, \Delta CIE_y]$ space. It can be seen that some noninferior solutions are outside the feasible region represented by the red dotted box and do not meet the optimization requirements. The noninferior solution with the highest CE is used as an example, which is indicated by a red asterisk in Fig. 6. The corresponding optimization parameters are $\mathbf{d}_A = [22.94, 5.06, 61.43, 43.50]$ nm. The wide FOV optical characteristics of this noninferior solution are $CE(0^\circ) = 101.47$ cd/A, $EQE = 25.9\%$, $JNCD_{\max} = 0.6$, but $\Delta CIE_x > 0.05$. Although the efficiency is improved, the chroma is poor.

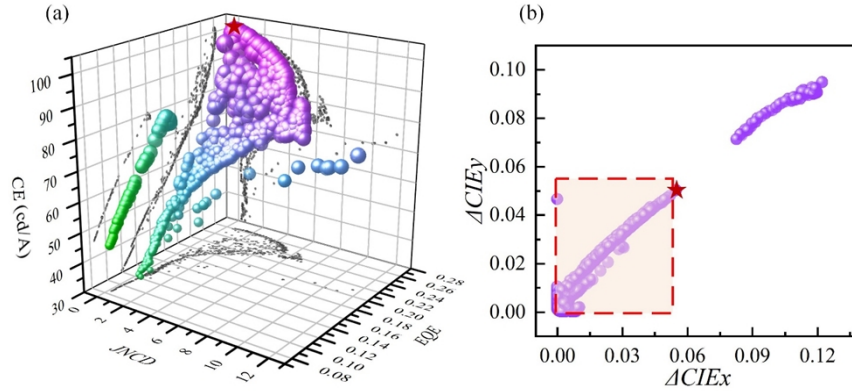


Fig. 6. Results of the multi-objective optimization based on the GA for the G-BOLED over wide FOV. (a) Noninferior solutions in $[CE, JNCD, EQE]$ space; (b) noninferior solutions in $[\Delta CIE_x, \Delta CIE_y]$ space. The red asterisked point represents the noninferior solution with the highest CE .

4.2. Design of stable OLEDs considering the thickness tolerance

As mentioned in Sec. 2.3, we give the thresholds for each objective separately, and divide each of them into three levels (A_i, B_i, C_i). The intervals between the A and B levels of objective $F_1(CE)$, $F_2(JNCD)$, and $F_{4,5}(CIE_x, CIE_y)$ are 90 cd/A, 4, and 0.05, respectively. The intervals between the B and C levels of objective F_1, F_2 , and $F_{4,5}$ are 60 cd/A, 6, and 0.1, respectively. Since the $CE(F_1)$ and $EQE(F_3)$ are positively correlated as shown in Fig. 6(a), when $F_1(CE) > 60$ cd/A, $F_3(EQE) > 0.2$. The constraint on $F_3(EQE)$ is omitted here, which does not affect the division of preference regions. Thus, the five preferred regions of the noninferior solutions can be expressed as: $\Omega_1 = \{F_1 \mid F_1 > 90 \text{ cd/A}\} \cap \{F_2 \mid F_2 < 4\} \cap \{F_{4,5} \mid F_{4,5} < 0.05\}$, $\Omega_2 = \{F_1 \mid 60 < F_1 < 90 \text{ cd/A}\} \cap \{F_2 \mid F_2 < 4\} \cap \{F_{4,5} \mid F_{4,5} < 0.05\}$, $\Omega_3 = \{F_1 \mid F_1 > 60 \text{ cd/A}\} \cap \{F_2 \mid 4 < F_2 < 6\} \cap \{F_{4,5} \mid F_{4,5} < 0.05\}$, $\Omega_4 = \{F_1 \mid F_1 < 60 \text{ cd/A}\} \cap \{F_2 \mid F_2 < 6\} \cap \{F_{4,5} \mid F_{4,5} < 0.05\}$, $\Omega_5 = \Omega - \Omega_1 - \Omega_2 - \Omega_3 - \Omega_4$. The thickness distributions corresponding to different preferred regions of the noninferior solutions are shown in Fig. 7. Points with different colors stand for different preferred regions of the noninferior solutions, and the color shade indicates the concentration degree. For all noninferior solutions, the ETL thickness can be in the range of 20~70 nm or

140~200 nm, the EBL thickness can vary from 0 to 180 nm, the HIL thickness can vary from 30 nm to 180 nm, while the HTL thickness needs to be less than 100 nm. The ETL thickness has the greatest impact on the performances of the G-BOLED, and when d_{ETL} falls in the range of 140~200 nm, the optical performances are poor. The “Best” and “better” preferred regions are more concentrated than others. The thickness ranges of the “Best” preferred region can be roughly described as: $20 < d_{ETL} < 40$ nm, $5 < d_{EBL} < 20$ nm, $30 < d_{HTL} < 70$ nm, and $40 < d_{HIL} < 70$ nm. It should be noted that points in Figs. 7(a)–(f) are related to each other, and there is one-to-one correspondence between them. For example, the red asterisked points in Figs. 7(a)–(f) all correspond to the highest CE solution with thicknesses $\mathbf{d}_A = [22.94, 5.06, 61.43, 43.50]$ nm.

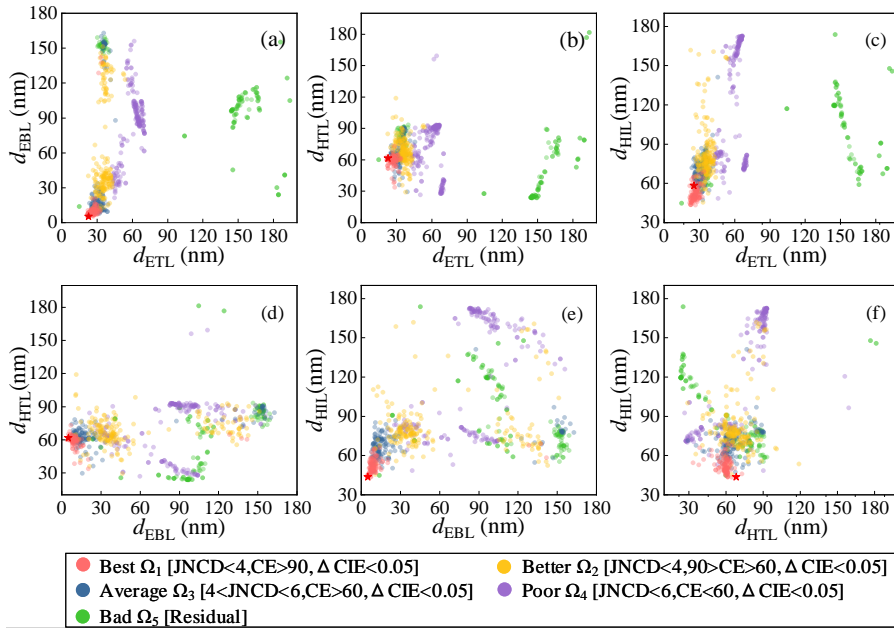


Fig. 7. Thickness distributions corresponding to different preferred regions of noninferior solutions: (a) in $[d_{ETL}, d_{EBL}]$ space; (b) in $[d_{ETL}, d_{HTL}]$ space; (c) in $[d_{ETL}, d_{HIL}]$ space; (d) in $[d_{EBL}, d_{HTL}]$ space; (e) in $[d_{EBL}, d_{HIL}]$ space; (f) in $[d_{HTL}, d_{HIL}]$ space. The red asterisked point represents the noninferior solution with the highest CE.

To guarantee the quality of the optimized devices and obtain the thickness tolerances, we performed a statistical correlation analysis for the film thicknesses of the “Best” preferred region. Figure 8 shows the statistical distributions of film thicknesses. The bar height indicates the numbers of the thickness occurring within the “Best” preferred region shown in Fig. 7. Since most noninferior solutions are not integers, the data is rounded for the statistical analysis. The thickness distribution of each layer can be well fitted by the Gaussian distribution function, as shown in Fig. 8, and the main fitting parameters are shown in Table 1. The MSE describes the degree of difference between the fitted Gaussian curve and the actual thickness distribution, and the smaller the MSE, the better the fitting. However, it is not enough to only judge the accuracy of the fitting using the MSE. It is also hoped that the function can capture the features of the data, such as distribution, monotonicity, etc., but whether the function captures these features cannot be judged by the MSE. The R-Square, also called Goodness of Fit, can make up for the above limits. If R-Square is close to 1, the functions explain the features of the data well. Generally, R-Square > 0.4 is acceptable. For all the four fittings in our analysis, the MSE values are less than 5, and the R-Square values are close to 1, indicating that the Gaussian functions can

describe the thickness distributions well. Here, μ and σ are the mathematical expectation and the standard deviation, which determine the tolerance of the film thickness. The film thickness tolerances of the four optimized layers are: $T_{\text{ETL}} = [18.49, 33.97]$ nm, $T_{\text{EBL}} = [2.46, 14.41]$ nm, $T_{\text{HTL}} = [56.47, 63.90]$ nm, $T_{\text{HIL}} = [36.21, 65.49]$ nm. In the practical process of preparing the OLED, if a $\pm 5\%$ fluctuation in the film thickness is taken, the target values of thicknesses can fall within the following range: $d_{\text{ETL}}^{\text{set}} = [19.46, 32.35]$ nm, $d_{\text{EBL}}^{\text{set}} = [2.59, 13.72]$ nm, $d_{\text{HTL}}^{\text{set}} = [59.44, 60.86]$ nm, $d_{\text{HIL}}^{\text{set}} = [38.17, 62.37]$ nm.

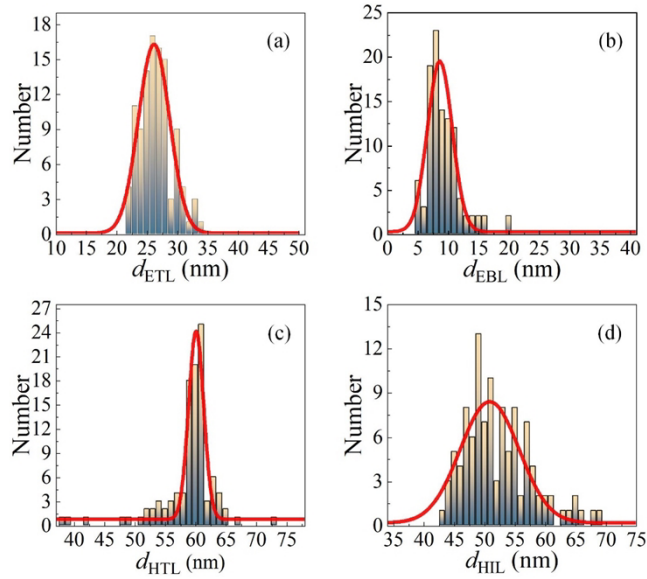


Fig. 8. Statistical thickness distributions for the “Best” preferred noninferior solutions of the G-BOLED over wide FOV: (a) ETL; (b) EBL; (c) HTL; (d) HIL.

Table 1. Main fitting parameters of Gaussian functions for film thickness distributions

Layer	μ [nm]	σ [nm]	MSE	R-Square
ETL	26.23	2.58	1.8	0.92
EBL	8.438	1.99	2.65	0.90
HTL	60.19	1.24	3.11	0.88
HIL	50.88	4.87	2.32	0.77

The above proposed film thickness tolerance covers the thickness distribution range of the “Best” preferred region and also considers process errors. However, in multivariate optimization, multiple parameters change simultaneously, and they are not independent of each other and have mutual influences. Therefore, the correlation coefficient is introduced to describe the variation relationship between the film thicknesses. The calculated thickness correlation coefficients are $\text{Corr}(d_{\text{ETL}}, d_{\text{EBL}}) = 0.3691$, $\text{Corr}(d_{\text{ETL}}, d_{\text{HTL}}) = -0.1650$, $\text{Corr}(d_{\text{ETL}}, d_{\text{HIL}}) = 0.2599$, $\text{Corr}(d_{\text{EBL}}, d_{\text{HTL}}) = -0.6334$, $\text{Corr}(d_{\text{EBL}}, d_{\text{HIL}}) = 0.3586$, and $\text{Corr}(d_{\text{HTL}}, d_{\text{HIL}}) = -0.3529$. It can be seen that d_{ETL} and d_{HTL} , d_{EBL} and d_{HTL} , d_{HTL} and d_{HIL} show certain degrees of negative correlations. While d_{ETL} and d_{EBL} , d_{ETL} and d_{HIL} , d_{EBL} and d_{HIL} are positively correlated. Positively correlated film thicknesses should have the same variation trend, while negatively correlated film thicknesses have opposite variation trends. The d_{EBL} and d_{HTL} exhibit the strongest linear correlation with a correlation coefficient of -0.6334 , which should be paid more

attention to in the optimization. To get an OLED with the “Best” performance, the thicknesses of the four optimized layers can be set as $\mathbf{d}_B = [26.23, 8.44, 60.19, 50.88]$ nm, namely the mathematical expectation values μ . If there is a little deviation in the thickness of one layer, such as the influence of the electrical characteristics of the device, the thickness of one layer cannot be set to the mathematical expectation value, then the thicknesses of other layers should be adjusted accordingly. If d_{ETL} is reduced, d_{EBL} and d_{HIL} should be appropriately reduced, and d_{HTL} should be appropriately increased. For example, for the structure indicated by the red asterisk in Fig. 7, the thickness of the ETL is less than μ_{ETL} . Therefore, other thicknesses should be adjusted. The target value of the thickness should fall within the range of d^{set} , while d_{HTL} in \mathbf{d}_A is not fallen in d^{set}_{HTL} , and the correction of \mathbf{d}_A according to the correlation coefficient and d^{set} can be expressed as $\mathbf{d}_C = [22.6, 8.2, 60.2, 47.4]$ nm. Namely, device C is the improved structure of device A considering the correlation between the film thicknesses, and it is more stable than device A.

4.3. Verification

The reliability and effectiveness of the proposed method are verified through simulations and experiments. Firstly, we performed high-throughput simulations to verify the stability of the structure with the thickness fluctuations in the process. The commercial software OFSS 1.0 (Wuhan Yuwei Optical Software Co., Ltd.) is used to perform the optical simulations. Devices A, B and C respectively with thicknesses $\mathbf{d}_A = [22.94, 5.06, 61.43, 43.50]$ nm, $\mathbf{d}_B = [26.23, 8.44, 60.19, 50.88]$ nm and $\mathbf{d}_C = [22.6, 8.2, 60.2, 47.4]$ nm are analyzed via simulations. Thickness fluctuations in simulations are set as $\pm 5\%$. Then, the rounded thickness ranges of device A can be expressed as $21 \leq d_{ETL} \leq 25$ nm, $4 \leq d_{EBL} \leq 6$ nm, $58 \leq d_{HTL} \leq 65$ nm, and $41 \leq d_{HIL} \leq 46$ nm. The rounded thickness ranges of device B can be expressed as: $24 \leq d_{ETL} \leq 28$ nm, $8 \leq d_{EBL} \leq 9$ nm, $57 \leq d_{HTL} \leq 64$ nm, and $48 \leq d_{HIL} \leq 53$ nm. The rounded thickness ranges of device C can be expressed as $21 \leq d_{ETL} \leq 24$ nm, $7 \leq d_{EBL} \leq 9$ nm, $57 \leq d_{HTL} \leq 64$ nm, and $45 \leq d_{HIL} \leq 50$ nm. Simulations are performed by varying the thicknesses of the referred four layers within the above fluctuation ranges simultaneously with an interval of 1 nm. Other parameters involved in the simulations are set as the same as those of the initial device.

Figure 9 shows simulation results about the chromaticity variation (i.e., ΔCIE) for these devices when thicknesses fluctuate. For device A, among 720 sets of noninferior solutions, 387 sets of solutions satisfy the “Best” preferred region strictly, accounting for 53.75%. For device B, all the 480 noninferior solutions obtained from the simulations satisfy the “Best” preferred region strictly, accounting for 100%. For device C, 576 noninferior solutions are obtained from the simulations, and 533 of them strictly satisfy the “Best” preferred region, accounting for 92.53%. The low percentages of the “Best” preferred region for device A and C are mainly due to the large deviation of CIE in the normal direction when the layer thicknesses of the devices fluctuate, as shown in Figs. 9(a) and 9(c), while the CIE of device B meets all requirements, as shown in Fig. 9(b). The wide FOV optical characteristics of device A are not stable enough, which will result in the degradation of the performance and the increase of cost. It should be noted that not all devices within the thickness tolerance will show the best performance. To obtain a high-performance device, the thickness of each layer should be well-designed by considering the correlation coefficient, just like device C.

Experiments corresponding to the high-throughput simulations are difficult to complete in the laboratory, therefore just one of the optimized devices is prepared to demonstrate the feasibility of the proposed optimization and analysis method. Since the wide FOV optical characteristics of device B is the most stable compared to device A and device C, device B is prepared in the laboratory, and its optical characteristics were measured and compared with the initial G-BOLED device. The target thicknesses of device B can be described as $\mathbf{d}_B = [26.23, 8.44, 60.19, 50.88]$ nm. Due to the processing errors, the actual thicknesses may deviate from their target values.

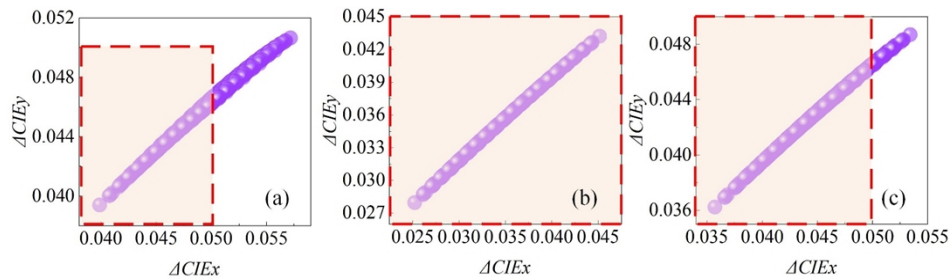


Fig. 9. Simulated chromaticity variation of OLED devices with thickness fluctuations: (a) device A; (b) device B; (c) device C. The red dotted box indicates the range of feasible solutions, i.e., $\Delta CIE_x, \Delta CIE_y \leq 0.05$.

The actual thicknesses are measured by the spectroscopic ellipsometer and can be described as $\mathbf{d}_{\text{actual}} = [26.32, 8.54, 63.10, 49.98]$ nm. The wide FOV optical characteristics of the two devices are measured and comparatively presented in Fig. 10. Figure 10(a) shows the measured luminescence spectra in the normal direction of the OLED devices. It can be observed that compared with the initial G-BOLED device, the peak intensity of device B in the normal direction increases by 1.6 times, and additionally the half-peak width is narrower, indicating that the optimized device has a higher *CE* in the normal direction with a purer chromaticity. The variation curves of *CE* versus the view angles are shown in Fig. 10(b). Over the whole FOV angle, the *CE* of device B is improved at least 20 cd/A compare with the initial device. For example, the *CE* of device B and initial device are 69.56 cd/A and 90.86 cd/A at the normal view angle, respectively. Then, we measured the *CIE* and *JNCD* of the devices over wide FOV, which are the most concerning parameters for OLEDs in wide FOV applications, and results are shown in Figs. 10(c) and 10(d). It can be seen that the color shift of device B is noticeably smaller than that of the initial device, and the chromaticity bias cannot be distinguished by human eyes since the *JNCD* is less than 1.5 over 0 to 60°. Thus, it can be concluded that the angle-dependent chromaticity is alleviated via optimizing the device structure. The measured *EQE* of the initial device and device B are 19.9% and 23.9%, respectively. The *EQE* of device B has been relatively improved by over 20% compared with the initial device.

In addition, we also measured the performance of the two devices at different voltages. The J-V-L curves of initial and optimized OLEDs are shown in Fig. 11(a). It is found that the electrical performance of the optimized device has changed compared with the initial device. Under the same voltage, the Luminesce and Current densities of the optimized device are greater than those of the initial device. When the current density is 10mA/m², the voltage of the initial device is 4.18, and the voltage of the optimized device is 4.09. Figure 11(b) shows the current efficiency and power efficiency as a function of voltage. It can be seen that the current efficiency and power efficiency of the initial and the optimized device decrease as the voltage increases. However, the current efficiency and power efficiency of optimized device under different voltages are larger than that of the initial device. For the optimized device, there are some deviations between the simulation results and the measured results, which is caused by the change of the electrical properties of the device.

It should be noted that in this paper we only take the above device as an example to verify the correctness and effectiveness of proposed method. The above device is a weak cavity structure, which may be not-representative because the off-angle issue is more severe in strong cavity OLEDs. But the proposed method itself is general, and can be applied to different OLED devices including both weak-cavity and strong-cavity structures. In future work, we will keep on optimizing a strong cavity OLED, and conduct systematic experiments.

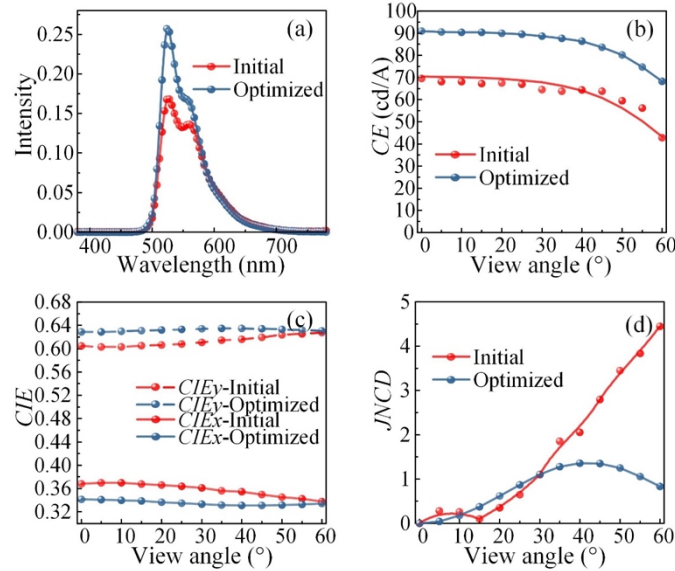


Fig. 10. The comparison of initial G-BOLED and device B. (a) The luminescence spectroscopy of initial and optimized devices in the normal direction. (b) The CE of initial and optimized devices over wide FOV. (c) The CIE of initial and optimized devices over wide FOV. (d) The JNCD of the initial and optimized devices over wide FOV. The dots represent the measured data, and the line is the trend of the measured data.

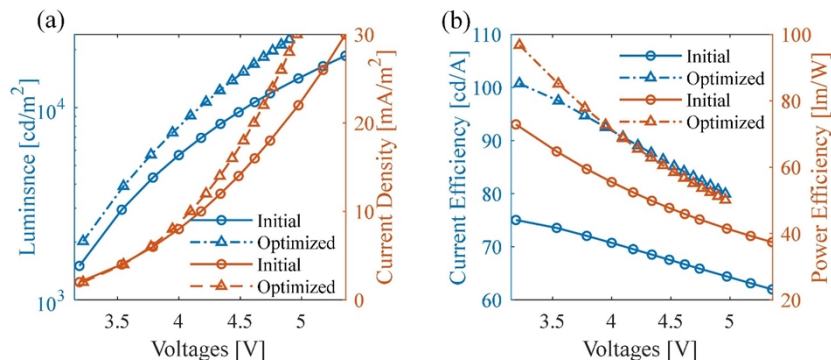


Fig. 11. The device performance of initial and optimized devices. (a) J-V-L curves; (b) CE-V-PE curves.

5. Conclusion

In summary, a multi-parameter and multi-objective optimization and analysis method is proposed to simultaneously alleviate the angle-dependent characteristics and improve the structural stability of stratified OLEDs over wide FOV considering thickness tolerance. Firstly, key parameters, including the *EQE*, *CE*, *JNCD*, and *CIE*, are defined using the angle-dependent luminescence spectra to describe the optical performances of the OLED device over wide FOV. Subsequently, a criterion based on the GA is defined to deal with the multi-parameter and multi-objective optimization problem of OLEDs over wide FOV. Finally, by defining and analyzing the distributions of preference regions of the GA output noninferior solutions and the correlation coefficients between layer thicknesses, appropriate thickness tolerances can be determined to achieve stable structures for the OLED device.

High-throughput simulations are performed on a typical G-BOLED to demonstrate the effectiveness and great potential of the proposed methods. Results show that key performances of the optimized device have been simultaneously improved compared with the initial device. When $\pm 5\%$ thickness fluctuations are assumed in the practical production, the output noninferior solutions of the optimization considering thickness tolerances 100% strictly satisfy the “Best” preferred region, compared with a proportion of 53.75% for those without considering thickness tolerances. In addition, when the structure is adjusted according to the correlation between the layer thicknesses, the proportion of the noninferior solutions that satisfy the “Best” preferred region is notably increased from 53.75% to 92.5%. These results indicate that with the proposed methods, we can design high-performance OLED device with a stable structure considering the thickness fluctuations in the practical production process. Finally, the optimized device with stable structure is prepared and characterized to give an experimental verification. Experimental results indicate that compared with the initial G-BOLED, the *CE* of the optimized device is improved by 30% in the normal direction, the *EQE* is improved by over 20% and the angular dependence of chromaticity is noticeably alleviated with the $JNCD_{\max}$ is reduced from 4.45 to 1.36.

Importantly, the thickness tolerance is introduced to evaluate and improve the structure stability of the OLED device considering thickness fluctuations in the practical production process, and it is helpful in improving production yield. Therefore, it can be concluded that the propose optimization method can be well applied to design a high-performance OLED over wide FOV with a stable structure, and it has promising applications in practical production, especially for wide FOV usage scenarios and large-size panels.

Funding. National Natural Science Foundation of China (51727809, 51805193); Key Research and Development Plan of Hubei Province (2021BAA013); Natural Science Foundation of Hubei Province (2021CFB322); Fundamental Research Funds for the Central Universities (2021XXJS113).

Acknowledgments. The authors thank the technical support from the Experiment Centre for Advanced Manufacturing and Technology in School of Mechanical Science & Engineering of HUST.

Disclosures. The authors declare no conflicts of interest.

Data availability. Data underlying the results presented in this paper are not publicly available at this time but may be obtained from the authors upon reasonable request.

References

1. H.-W. Chen, J.-H. Lee, B.-Y. Lin, S. Chen, and S.-T. Wu, “Liquid crystal display and organic light-emitting diode display: present status and future perspectives,” *Light: Sci. Appl.* **7**(3), 17168 (2018).
2. J. Song, H. Lee, E. G. Jeong, K. C. Choi, and S. Yoo, “Organic Light-Emitting Diodes: Pushing toward the Limits and Beyond,” *Adv. Mater.* **32**(35), 1907539 (2020).
3. S.-J. Zou, Y. Shen, F.-M. Xie, J.-D. Chen, Y.-Q. Li, and J.-X. Tang, “Recent advances in organic light-emitting diodes: toward smart lighting and displays,” *Mater. Chem. Front.* **4**(3), 788–820 (2020).
4. G. Huseynova, J. H. Lee, Y. H. Kim, and J. Lee, “Transparent Organic Light-Emitting Diodes: Advances, Prospects, and Challenges,” *Adv. Opt. Mater.* **9**(14), 2002040 (2021).

5. H. Uoyama, K. Goushi, K. Shizu, H. Nomura, and C. Adachi, "Highly efficient organic light-emitting diodes from delayed fluorescence," *Nature* **492**(7428), 234–238 (2012).
6. C. Adachi, "Third-generation organic electroluminescence materials," *Jpn. J. Appl. Phys.* **53**(6), 060101 (2014).
7. J. Guo, Z. Zhao, and B. Z. Tang, "Purely Organic Materials with Aggregation-Induced Delayed Fluorescence for Efficient Nondoped OLEDs," *Adv. Opt. Mater.* **6**(15), 1800264 (2018).
8. Y. Hu, W. Cai, L. Ying, D. Chen, X. Yang, X.-F. Jiang, S. Su, F. Huang, and Y. Cao, "Novel efficient blue and bluish-green light-emitting polymers with delayed fluorescence," *J. Mater. Chem. C* **6**(11), 2690–2695 (2018).
9. D. Sun, S. M. Suresh, D. Hall, M. Zhang, C. Si, D. B. Cordes, A. M. Z. Slawin, Y. Olivier, X. Zhang, and E. Zysman-Colman, "The design of an extended multiple resonance TADF emitter based on a polycyclic amine/carbonyl system," *Mater. Chem. Front.* **4**(7), 2018–2022 (2020).
10. J. H. Yun, K. H. Lee, J. Y. Lee, and W. P. Hong, "Benzofurodibenzofuran as a universal chemical platform of highly efficient sky-blue thermally activated delayed fluorescence emitters and hosts," *Chem. Eng. J.* **411**, 128550 (2021).
11. J.-S. Huh, M. J. Sung, S.-K. Kwon, Y.-H. Kim, and J.-J. Kim, "Highly Efficient Deep Blue Phosphorescent OLEDs Based on Tetradentate Pt(II) Complexes Containing Adamantyl Spacer Groups," *Adv. Funct. Mater.* **31**(23), 2100967 (2021).
12. Y. Liu, X. Xiao, Y. Ran, Z. Bin, and J. You, "Molecular design of thermally activated delayed fluorescent emitters for narrowband orange-red OLEDs boosted by a cyano-functionalization strategy," *Chem. Sci.* **12**(27), 9408–9412 (2021).
13. M. Mao, T.-L. Lam, W.-P. To, X. Lao, W. Liu, S. Xu, G. Cheng, and C.-M. Che, "Stable, High-Efficiency Voltage-Dependent Color-Tunable Organic Light-Emitting Diodes with a Single Tetradentate Platinum(II) Emitter Having Long Operational Lifetime," *Adv. Mater.* **33**(2), 2004873 (2021).
14. C. Xu, L.-B. Niu, Y.-C. Qian, L. Wen, Y.-Q. Xiong, H.-N. Peng, and Y.-X. Guan, "Research on Fe(NH₂trz)₃center dot(BF₄)₂ doped polyfluorene organic light-emitting devices," *Acta Phys. Sin.* **70**(7), 077202 (2021).
15. W. S. Cho, J. Y. Park, S. Baek, C. S. Choi, S.-H. Cho, K. Hong, and J.-L. Lee, "Completely Hazy and Transparent Films by Embedding Air Gaps for Elimination of Angular Color Shift in Organic Light-Emitting Diodes," *ACS Appl. Mater. Interfaces* **13**(33), 39660–39670 (2021).
16. B. Pyo, C. W. Joo, H. S. Kim, B.-H. Kwon, J.-I. Lee, J. Lee, and M. C. Suh, "A nanoporous polymer film as a diffuser as well as a light extraction component for top emitting organic light emitting diodes with a strong microcavity structure," *Nanoscale* **8**(16), 8575–8582 (2016).
17. Q.-D. Ou, L. Zhou, Y.-Q. Li, J.-D. Chen, C. Li, S. Shen, and J.-X. Tang, "Simultaneously Enhancing Color Spatial Uniformity and Operational Stability with Deterministic Quasi-periodic Nanocone Arrays for Tandem Organic Light-Emitting Diodes," *Adv. Opt. Mater.* **3**(1), 87–94 (2015).
18. Y.-H. Wang, H.-F. Cui, Y.-F. Zhang, and A.-W. Li, "Improved viewing characteristics of red emission top-emitting organic light-emitting devices by integrating grating," *Opt. Eng.* **52**(8), 080502 (2013).
19. D. Samigullina, P.-A. Will, L. Galle, S. Lenk, J. Grothe, S. Kaskel, and S. Reineke, "Parameter Optimization of Light Outcoupling Structures for High-Efficiency Organic Light-Emitting Diodes," *J. Appl. Phys.* **128**(18), 185501 (2020).
20. J.-B. Kim, J.-H. Lee, C.-K. Moon, K.-H. Kim, and J.-J. Kim, "Highly enhanced light extraction from organic light emitting diodes with little image blurring and good color stability," *Org. Electron.* **17**, 115–120 (2015).
21. N. S. Kim, D. Y. Kim, J. H. Song, and M. C. Suh, "Improvement of viewing angle dependence of bottom-emitting green organic light-emitting diodes with a strong microcavity effect," *Opt. Express* **28**(21), 31686–31699 (2020).
22. G. Chen, Y. Weng, X. Lai, W. Wang, X. Zhou, Q. Yan, T. Guo, Y. Zhang, and C. Wu, "Design and fabrication of hybrid MLAs/gratings for the enhancement of light extraction efficiency and distribution uniformity of OLEDs," *Opt. Express* **29**(16), 25812–25823 (2021).
23. H. Riel, S. Karg, T. Beierlein, W. Rieß, and K. Neyts, "Tuning the emission characteristics of top-emitting organic light-emitting devices by means of a dielectric capping layer: An experimental and theoretical study," *J. Appl. Phys.* **94**(8), 5290–5296 (2003).
24. C.-C. Wu, C.-L. Lin, P.-Y. Hsieh, and H.-H. Chiang, "Methodology for optimizing viewing characteristics of top-emitting organic light-emitting devices," *Appl. Phys. Lett.* **84**(20), 3966–3968 (2004).
25. J.-B. Kim, J.-H. Lee, C.-K. Moon, and J.-J. Kim, "Highly efficient inverted top emitting organic light emitting diodes using a transparent top electrode with color stability on viewing angle," *Appl. Phys. Lett.* **104**(7), 073301 (2014).
26. T. Schwab, S. Schubert, S. Hofmann, M. Fröbel, C. Fuchs, M. Thomschke, L. Müller-Meskamp, K. Leo, and M. C. Gather, "Highly Efficient Color Stable Inverted White Top-Emitting OLEDs with Ultra-Thin Wetting Layer Top Electrodes," *Adv. Opt. Mater.* **1**(10), 707–713 (2013).
27. T. Schwab, S. Schubert, L. Müller-Meskamp, K. Leo, and M. C. Gather, "Eliminating Micro-Cavity Effects in White Top-Emitting OLEDs by Ultra-Thin Metallic Top Electrodes," *Adv. Opt. Mater.* **1**(12), 921–925 (2013).
28. C. Dong, X. Fu, S. Amoah, A. Rozelle, D. H. Shin, A. Salehi, J. Mendes, and F. So, "Eliminate angular color shift in top-emitting OLEDs through cavity design," *J. Soc. Inf. Disp.* **27**(8), 469–479 (2019).
29. IHS Markit, "An unmatched combination of information, analytics and expertise", <https://ihsmarkit.com/index.html>.
30. C.-L. Lin, H.-C. Chang, K.-C. Tien, and C.-C. Wu, "Influences of resonant wavelengths on performances of microcavity organic light-emitting devices," *Appl. Phys. Lett.* **90**(7), 071111 (2007).
31. E. Kim, J. Chung, J. Lee, H. Cho, N. S. Cho, and S. Yoo, "A systematic approach to reducing angular color shift in cavity-based organic light-emitting diodes," *Org. Electron.* **48**, 348–356 (2017).

32. G. Tan, J.-H. Lee, S.-C. Lin, R. Zhu, S.-H. Choi, and S.-T. Wu, "Analysis and optimization on the angular color shift of RGB OLED displays," *Opt. Express* **25**(26), 33629 (2017).
33. C. Dong, X. Fu, L. Cao, S. Amoah, K. Gundogdu, J. Li, and F. So, "Multi-mode Organic Light-Emitting Diode to Suppress the Viewing Angle Dependence," *ACS Appl. Mater. Interfaces* **12**(28), 31667–31676 (2020).
34. X. Ke, H. Gu, L. Chen, X. Zhao, J. Tian, Y. Shi, X. Chen, C. Zhang, H. Jiang, and S. Liu, "Multi-objective collaborative optimization strategy for efficiency and chromaticity of stratified OLEDs based on an optical simulation method and sensitivity analysis," *Opt. Express* **28**(19), 27532–27546 (2020).
35. X. Ke, H. Gu, X. Zhao, X. Chen, Y. Shi, C. Zhang, H. Jiang, and S. Liu, "Simulation method for study on outcoupling characteristics of stratified anisotropic OLEDs," *Opt. Express* **27**(16), A1014–A1029 (2019).
36. M. Flaemmich, D. Michaelis, and N. Danz, "Accessing OLED emitter properties by radiation pattern analyses," *Org. Electron.* **12**(1), 83–91 (2011).
37. J. Ge, Y. Qiu, C. Wu, and G. Pu, "Summary of genetic algorithms research," *Application Research of Computers* **25**(10), 2911–2916 (2008).
38. S. Katoch, S. S. Chauhan, and V. Kumar, "A review on genetic algorithm: past, present, and future," *Multimed Tools Appl* **80**(5), 8091–8126 (2021).
39. S. Liu, X. Chen, and C. Zhang, "Development of a broadband Mueller matrix ellipsometer as a powerful tool for nanostructure metrology," *Thin Solid Films* **584**, 176–185 (2015).
40. H. Gu, X. Chen, H. Jiang, C. Zhang, and S. Liu, "Optimal broadband Mueller matrix ellipsometer using multi-waveplates with flexibly oriented axes," *J. Opt.* **18**(2), 025702 (2016).
41. N. Jiang, H.-N. Yang, J.-X. Man, T. Zhang, S.-J. He, D.-K. Wang, and Z.-H. Lu, "Determination of emitting dipole orientation in organic light emitting diodes," *Org. Electron.* **78**, 105611 (2020).
42. Y. Sukegawa, Y. Sakai, and D. Yokoyama, "Model-free analysis of molecular orientation in amorphous organic semiconductor films for understanding its formation dynamics: Methods and systematic investigation," *Org. Electron.* **100**, 106377 (2022).